Journal of Advanced Ceramics
先进陶瓷
ISSN 2226-4108
CN 10-1154/TQ
清华大学出版社 Tsinghua University Press
SciOpen

*J Adv Ceram* 2026, **15**: 9221371

https://doi.org/10.26599/JAC.2026.9221371

Research Article

# Broadband-NIR Luminescent $MgNb_2O_6:Cr^{3+}$ transparent glass ceramics fabricated by co-melting and controlled crystallization

Jinliang Huang[1], Peihong Shi[2], Junhua Lin[3], Weijie Yan[1], Libin Xia[1,4,5,*] , Xinyu Ye[3,4,*]

[1]*School of Carbon Neutrality, Jiangxi University of Science and Technology, Nanchang 330006, China*

[2]*School of Materials Science and Engineering, Jiangxi University of Science and Technology, Ganzhou 341000, China*

[3]*College of Rare Earths, Jiangxi University of Science and Technology, Ganzhou 341000, China*

[4]*Faculty of Metallurgy and Chemical Engineering, Jiangxi University of Science and Technology, Ganzhou 341000, China*

[5]*Jiangxi Provincial Key Laboratory of Functional Crystalline Materials Chemistry, Jiangxi University of Science and Technology, Ganzhou 341000, China*

*Corresponding author.

E-mail: L. Xia, tea_xia@126.com;

X. Ye, ye_xin_yu@126.com

Received: July 3, 2026; Revised: August 28, 2026; Accepted: September 4, 2026

**Abstract:** Heat accumulation and severe light scattering limit the applications of near-infrared phosphor-converted LEDs (NIR pc-LEDs) in the high-power field. Replacing phosphor encapsulation with $Cr^{3+}$-doped glass-ceramics (GCs) provides an effective solution. However, obtaining transparent GCs with high thermal quenching resistance remains challenging. In this work, a novel $Cr^{3+}$-doped $MgNb_2O_6$ GC was fabricated by co-melting and controlled crystallization using glass-forming and target-phase precursors. The resultant GCs possess acceptable transmittance and favorable thermal quenching resistance. By tuning the Mg/Nb ratio, a single $MgNb_2O_6$ crystalline phase was precipitated, and a two-step heat treatment optimized the GC transmittance. With nucleation temperature rising from 670 ℃ to 750 ℃ and crystallization temperature increasing from 820 ℃ to 960 ℃, crystallinity, grain size and luminous intensity gradually increase, whereas transmittance decreases monotonically. $Cr^{3+}$ are proposed to simultaneously occupy $Mg^{2+}$ and $Nb^{5+}$ sites in $MgNb_2O_6$. Broadband NIR emission covering 600–1300 nm with a full width at half maximum (FWHM) of 210 nm is achieved, arising from intermediate and weak crystal fields and moderate electron-phonon coupling. After nucleation at 730 ℃ and crystallization at 940 ℃, the optimized GC shows a transmittance of approximately 50% and a high absorptivity of 60.5%. The GC exhibits favorable thermal quenching resistance, retaining 67.5% initial luminous intensity at 373 K. The NIR LED device integrated with the $MgNb_2O_6$:$Cr^{3+}$ GC delivers an output power of 240.9 mW and a power conversion efficiency of 6.3%, demonstrating promising application prospects in night-vision illumination, food testing, biomedical and anti-counterfeiting fields.

**Keywords:** glass-ceramic; $MgNb_2O_6$:$Cr^{3+}$; biomedical; near-infrared



## 1. Introduction

Broadband near-infrared (NIR) light sources, characterized by strong tissue penetration and low scattering loss, have been widely applied in plant lighting, food detection, security monitoring, night-vision illumination, biomedical imaging, and non-invasive analysis [1,2]. Compared with traditional NIR light sources such as halogen-tungsten lamps and incandescent lamps, NIR phosphor-converted LEDs (pc-LEDs) have attracted extensive attention due to their compact structure, long lifetime and energy efficiency [3]. Rare-earth ions and transition metal ions are commonly used as activators in phosphors to achieve NIR emission, but they suffer from inherent drawbacks including unstable

valence states, limited emission bandwidth, weak blue-light absorption and low quantum efficiency [4]. In contrast, $Cr^{3+}$ can be well matched with commercial blue LED chips and exhibits widely tunable emission wavelengths [5]. However, conventional NIR pc-LEDs adopt a transmission-type packaging structure, in which micrometer-sized NIR phosphors (typically 5–50 μm) are dispersed in a polymer encapsulant and directly coated onto high-power blue LED chips [6]. This packaging configuration causes intense optical scattering owing to the large refractive index mismatch between the phosphors and encapsulants, leading to severe photon trapping within the composite layer and thus low NIR transmittance (< 10% in the 700–1000 nm range), which limits the output power [7,8]. Furthermore, the low thermal conductivity of the encapsulants causes severe heat accumulation, resulting in efficiency degradation of NIR pc-LEDs [9].

Glass-ceramics (GCs) integrate the structural advantages of crystalline phases (low phonon energy, high activator solubility, etc.) and the functional advantages of glasses (high optical transmittance, high thermal conductivity and excellent chemical durability), making them suitable substitutes for polymer encapsulation to overcome the limitations caused by low thermal conductivity and poor transmittance [10,11]. Among them, niobate silicate GCs stand out in the fields of ferroelectric, piezoelectric and luminescent materials due to their unique structure and excellent properties such as high strength, good chemical stability and high NIR transmittance [12,13]. To date, some GCs containing niobate crystalline phases have been reported. For example, GCs incorporating tungsten bronze-type $Ba_2NaNb_5O_{15}$ [14], perovskite-type $Ca_2LaNbO_6$ [15] and $Ba_2YNbO_6$ [16] crystalline phases have been doped with various activator ions to achieve luminescence at different wavelengths [17]. However, for the fabrication of these niobate-based GCs, previous works merely provide glass compositions without explaining the basis for compositional design, or directly employ the phosphor-in-glass (PiG) strategy. Few studies address the fabrication of GCs via tailored composition design for glass matrices and luminescent powder precursors. In addition, achieving favorable transparency in GCs remains a challenge due to light scattering caused by refractive index mismatch between crystals and glass, as well as grain coarsening during crystallization. Glass contains various oxides and its disordered structure also often leads to multiple crystalline phases during heat treatment, making it difficult to obtain the desired phase.

In this work, a strategy of co-melting and controlled crystallization using glass-forming and target-phase precursors is proposed. By precisely adjusting the Mg/Nb ratio to match the stoichiometry of the target phase and employing a two-step heat treatment, controllable precipitation of single-phase $MgNb_2O_6$ microcrystals with uniform size distribution is achieved. $Cr^{3+}$ are proposed to simultaneously substitute for $Mg^{2+}$ and $Nb^{5+}$ at octahedral sites in the lattice, and the GC exhibits a broadband NIR emission. The as-prepared GC possesses favorable thermal stability in comparison with most previously reported materials. The optimized NIR pc-LED device integrated with the optimized $MgNb_2O_6$:$Cr^{3+}$ GC and a blue LED chip exhibits great potential as a near-infrared light source for night-vision lighting and non-destructive security inspection.

## 2. Experimental section

### 2.1. Sample preparation

Based on the strategy of co-melting and controlled crystallization using glass-forming and target-phase precursors, the $SiO_2$-$Na_2O$ system was employed as the traditional glass matrix with a total molar content of 58 mol% (the molar ratio was approximately 3:1), and the remaining 42 mol% consisted of MgO and $Nb_2O_5$ derived from the target crystalline phase of $MgNb_2O_6$, with slight adjustments based on the stoichiometric ratio. Subsequently, a series of precursor glasses (PG) with different Mg/Nb ratios with compositions of $43SiO_2$–$x$MgO–$(42-x)Nb_2O_5$–$15Na_2O$–$0.1Cr_2O_3$ ($x$=12, 16, 20, 24) were prepared via a high-temperature melting method. The glass compositions are listed in Table 1, in which $Cr_2O_3$ is incorporated as an extra dopant. Raw materials were accurately weighed according to the composition ratios, finely ground in an agate mortar for 30 min, and the homogeneous mixtures were transferred into alumina crucibles and melted at 1550 ℃ for 2 h in a muffle furnace under an air atmosphere. The glass melt was rapidly poured onto a preheated copper plate and pressed into shape, then heat-treated at 550 ℃ and held for 2 h to fully release internal stress, yielding precursor glass (PG). The PG samples with different Mg/Nb ratios were embedded in alumina powder and heat-treated at 920 ℃ for 3 h, designated as GC-M12, GC-M16, GC-M20, and GC-M24, respectively. Using a two-step heat treatment process, the glass sample of M24 was subjected to nucleation treatment at 670, 690, 710, 730, and 750 ℃ for 12 h, respectively. The samples were named as MNO-670, MNO-690, MNO-710, MNO-730, and MNO-750. After the optimal nucleation temperature (NT) of 730 ℃, heat

treatment was performed at 820 ℃, 840 ℃, 860 ℃, 880 ℃, 900 ℃, 920 ℃, 940 ℃, and 960 ℃ for 3 h, named as GCM820, GCM840, GCM860, GCM880, GCM900, GCM920, GCM940, and GCM960, respectively. GCs with different $Cr^{3+}$ doping concentrations (from 0.05, 0.1, 0.15 to 0.2 mol%) based on GCM940 sample were named as GCM005, GCM01, GCM015, and GCM02, respectively. After cooling to room temperature in the furnace, the bulk PGs were cut, ground, and polished into samples with a thickness of 2.0 mm for subsequent optical measurements.

Table 1 Chemical composition of the precursor glasses (mol%)

| Samples number | $SiO_2$ | MgO | $Nb_2O_5$ | $Na_2O$ | $Cr_2O_3$ |
|---|---|---|---|---|---|
| M12 | 43 | 12 | 30 | 15 | 0.1 |
| M16 | 43 | 16 | 26 | 15 | 0.1 |
| M20 | 43 | 20 | 22 | 15 | 0.1 |
| M24 | 43 | 24 | 18 | 15 | 0.1 |

### 2.2. Characterization of sample performance

The crystalline phases of the samples were identified by X-ray powder diffraction (XRD, Bruker D8 Advance) with Cu Kα radiation (λ = 1.5406 Å), operating at 40 kV and 40 mA. Data were collected over a 2θ range of 10–80° at a scanning rate of 10 °/min. The microstructure and elemental distribution were examined using a field-emission scanning electron microscope (SEM, Sigma 500, Zeiss) equipped with an energy-dispersive X-ray spectrometer (EDS). Differential thermal analysis (DTA, DTG-60A H, Shimadzu) was conducted from 400 to 1000 ℃ at a heating rate of 10 ℃/min in air to determine the glass transition temperature ($T_g$) and crystallization peak temperature ($T_c$). Optical transmittance spectra in the 300–1400 nm range were recorded on a UV-Vis-NIR spectrophotometer (Lambda 950, PerkinElmer) at a scan speed of 2 nm/s. Photoluminescence (PL) excitation and emission spectra, as well as fluorescence decay curves, were measured on a fluorescence spectrometer (FLS980, Edinburgh Instruments) equipped with a 450 W xenon lamp as the excitation source and a microsecond pulsed lamp for lifetime measurements. Temperature-dependent PL spectra were acquired using a high-temperature accessory (TAP-02, Tianjin Orient KOJI) attached to the spectrometer. The electroluminescence performance of the NIR LED device was evaluated using a high-resolution spectroradiometer (HAAS-2000-IR1, Everfine).

## 3. Results and discussion

### 3.1. Glass properties and crystal structures

The DTA curve of PG-M24 is shown in Fig. 1a. As seen from the figure, the glass transition temperature ($T_g$) and the peak crystallization temperature ($T_c$) are 655 ℃ and 790 ℃, respectively. According to the $T_g$ and $T_c$, the initial heat treatment temperature is to be identified. Additionally, the $\Delta T$ between $T_c$ and $T_g$ is 135 ℃, indicating that the crystallization process of the PG is relatively controllable. Fig. 1b shows the XRD patterns of PG-M12 to PG-M24 samples, displaying amorphous "hump" peaks without obvious diffraction peaks, suggesting that no crystallization occurs in the glass. To investigate the effect of different Mg/Nb ratios, the XRD patterns of PG-M12 to PG-M24 after heat treatment at 920 ℃ for 3 h were characterized, and the results are displayed in Fig. 1c. As can be seen in the figure, the GC-M12 sample comprises two crystalline phases: $MgNb_2O_6$ (JCPDS No. 33-0875) and $Nb_2O_5$ (JCPDS No. 19-0864). As the MgO content increases from 12 to 24 mol%, the Mg/Nb ratio approaches the stoichiometric ratio of 1:2 for the target $MgNb_2O_6$ phase. Accordingly, the diffraction peaks of the $Nb_2O_5$ impurity phase gradually weaken and finally vanish completely when the MgO content reaches 24 mol%, yielding single-phase $MgNb_2O_6$. Simultaneously, the diffraction peak intensity of $MgNb_2O_6$ gradually increases, indicating that a higher MgO content promotes the combination of $Nb^{5+}$ with $Mg^{2+}$ to form the desired $MgNb_2O_6$ rather than remaining as $Nb_2O_5$. This compositional evolution clearly demonstrates the effectiveness of our strategy of incorporating the target crystalline phase composition into the glass matrix. By adjusting the Mg/Nb ratio in the precursor glass to match the stoichiometry of the target phase, the precipitation of a single desired crystalline phase can be controllably achieved, while avoiding unwanted impurity phases. Fig. 1d shows the images of as-prepared GCs under natural light (left side) and NIR light (right side), providing a more intuitive demonstration of the changes in glass transmittance. The transmittance of the samples under both natural light and NIR light gradually increases from GC-M12 to GC-M24, which is attributed to the gradual disappearance of the refractive index difference between different crystalline phases, reducing optical scattering. Meanwhile, since $Cr^{3+}$ absorbs light in different wavelength ranges under varying crystal field environments, the GCs gradually change in color from green to light brown [18,19]. The M24 sample exhibits relatively high transmittance and precipitates

a single crystalline phase. Therefore, M24 was selected for subsequent experiments to avoid the influence of impurity phases. The crystal structure diagram of $MgNb_2O_6$, as shown in Fig. 1e, belongs to the orthorhombic system (space group *Pbcn*, $a$ = 5.700 Å, $b$ = 14.193 Å, $c$ = 5.032 Å). Both $Mg^{2+}$ and $Nb^{5+}$ ions are coordinated with six $O^{2-}$ ions to form [$MgO_6$] and [$NbO_6$] octahedra, which are connected by sharing vertices or edges to form a two-dimensional layered structure. Considering the valence states and ionic radii of $Mg^{2+}$ (r = 0.72 Å when CN = 6), $Nb^{5+}$ (r = 0.64 Å when CN = 6), and $Cr^{3+}$ (r = 0.62 Å when CN = 6), the acceptable percentage difference does not exceed 30% [20]. The radius percentage difference ($D_r$) between $Cr^{3+}$ and the possible substituted ions ($Mg^{2+}$ and $Nb^{5+}$) can be calculated by the following formula [20]:

$$D_r = 100\% \times [R_m(CN) - R(CN)]/R_m(CN) \quad (1)$$

where $CN$ is the coordination number of the cation, $R_m(CN)$ is the radius of the potentially substituted ion ($Mg^{2+}$ and $Nb^{5+}$), and $R(CN)$ is the radius of the dopant ion ($Cr^{3+}$). The calculated $D_r$ values are 14% for $Mg^{2+}$ and 3% for $Nb^{5+}$, indicating that $Cr^{3+}$ ions may simultaneously substitute for the six-coordinated sites of $Mg^{2+}$ and $Nb^{5+}$ in $MgNb_2O_6$, which will be further analyzed in the subsequent section.

To achieve controllable crystallization and obtain more microcrystals with uniform distribution in the glass matrix, a two-step heat treatment process was subsequently applied to the glass of composition M24, making it necessary to determine suitable nucleation and crystallization temperatures. Generally, the optimal NT lies between $T_g$ and $T_g$ + 50 ℃. Then, temperatures of 670 ℃, 690 ℃, 710 ℃, 730 ℃, and 750 ℃ were selected as the NT, held for 12 h, and then crystallized at 920 ℃ for 3 h. The XRD patterns of the resulting GCs are shown in Fig. 1f. As seen from the inset, the glass prepared by the two-step method appears more transparent, which is attributed to the precipitation of more small crystal nuclei during the nucleation stage. Upon subsequent heating to the crystallization temperature, these small nuclei grow uniformly, leading to more homogeneous crystallization of the glass and a reduced refractive index difference between large and small grains. Additionally, the XRD patterns in the lower part of Fig. 1f show a few weak and broadened diffraction peaks of MgNb2O6, whose intensities increase with increasing temperature from 670 to 750 °C (without grain-growth treatment at 920 °C), indicating that grains gradually form and aggregate. The

subsequent spectral measurements (Figs. 4a and 4b) reveal that the 730 ℃ sample exhibits a slight reduction in PL intensity yet retains favorable transparency relative to the 750 ℃ sample. Therefore, 730 ℃ is chosen as the optimum nucleation temperature. After nucleation at 730 ℃ for 12 h, the samples were subjected to crystallization treatment at 820–960 ℃ in 20 ℃ increments for 3 h, and the corresponding XRD patterns are presented in Fig. 1g. The diffraction peak intensities significantly increase without the appearance of any other impurity peaks from GCM820 to GCM960, indicating an increasing degree of crystallization. The increase in the volume fraction of precipitated crystals exacerbates the mismatch of reflection coefficients between grains and grain boundaries, and between grains and the residual glass phase, thereby gradually reducing the transmittance of the GCs. Fig. 1h shows the XRD patterns of GCs doped with different concentrations of $Cr_2O_3$ (0.05, 0.1, 0.15, and 0.2 mol%) after nucleation at 730 ℃ for 12 h and heat treatment at 940 ℃ for 3 h. The diffraction peaks of all samples are consistent with the standard $MgNb_2O_6$ phase (JCPDS No. 33-0875), confirming that $Cr_2O_3$ doping does not alter the crystalline phase composition. This result indicates that $Cr^{3+}$ mainly enters the $MgNb_2O_6$ lattice through substitutional doping rather than forming a second phase. It is worth noting that the diffraction peak intensity shows a slight decreasing trend with increasing $Cr_2O_3$ content. High-concentration $Cr^{3+}$ doping increases the crystallization activation energy and inhibits ion migration, thereby transforming $Cr^{3+}$ from a nucleating agent into a network stabilizer, ultimately reducing the degree of crystallization [21,22]. A similar trend has been observed in other GCs. Fig. 1i shows photographs of the samples, providing a more intuitive view of the changes in glass transmittance. As the nucleation and crystallization temperatures increase, the transmittance of the glass under natural light gradually decreases, and similarly decreases under NIR light (the underlying text remains visible).

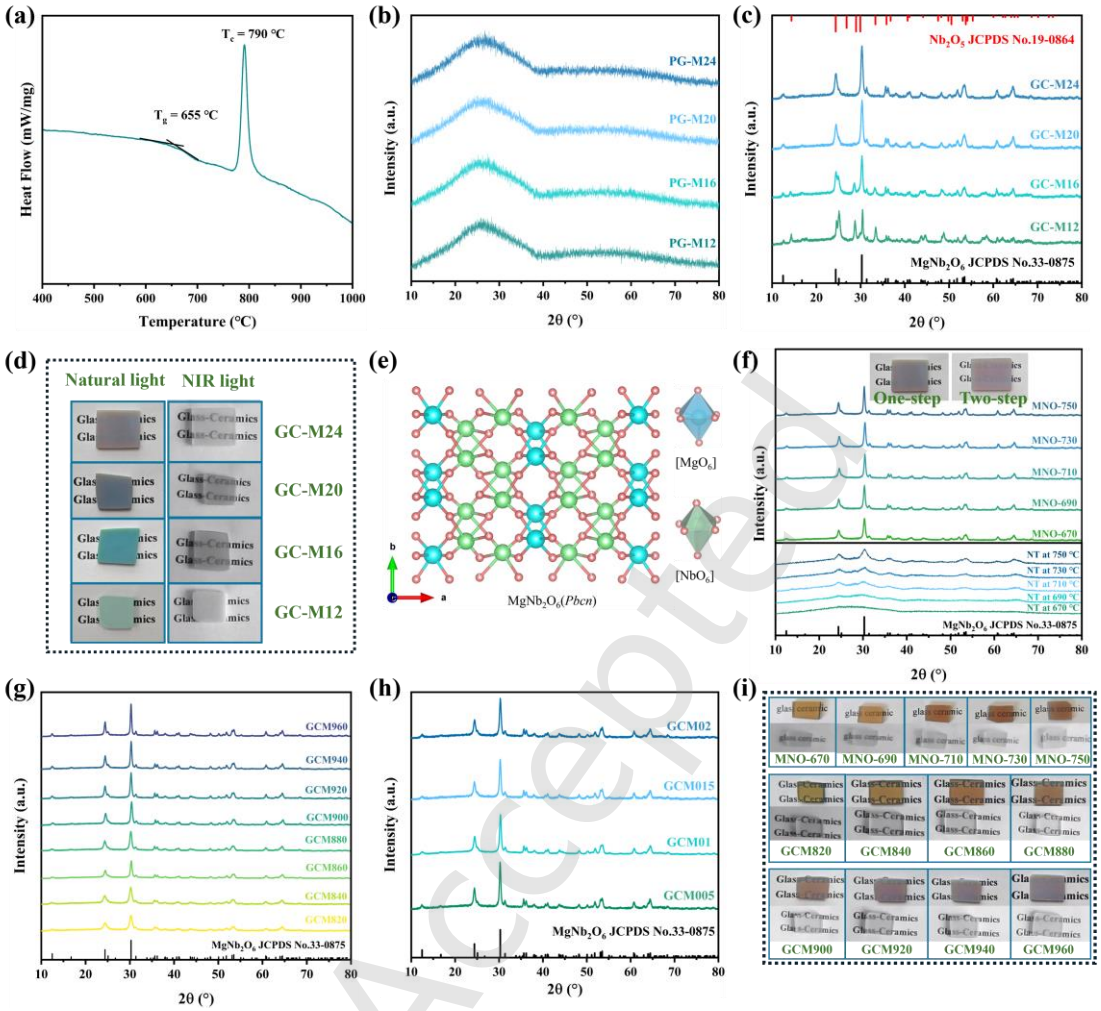


Fig. 1. (a) DTA curve of PG-M24. (b) XRD patterns of PG-M12 to PG-M24 and (c) GC-M12 to GC-M24. (d) Photographs of GC-M12 to GC-M24 samples (left: natural light, right: NIR light). (e) Crystal structure diagram of $MgNb_2O_6$. XRD patterns of GC-M24 at (f) different NT (the upper part: with crystallization at 920 °C for 3 h, insets: photographs in natural light; right: two-step method, lower: without crystallization treatment at 920 °C), (g) different crystallization temperatures, and (h) different $Cr^{3+}$ doping concentrations. (i) photographs of samples at different nucleation and crystallization temperatures (above: natural light, below: NIR light).

### 3.2. Microstructure morphology

As observed in the SEM images (Figs. 2a–b), all samples exhibit distinct crystal precipitation inside the glass matrix. GC-M12 (Fig. 2a) suffers from severe grain agglomeration and large grain sizes, which triggers intense light scattering and degrades transmittance. In comparison, GC-M24 (Fig. 2b) possesses relatively smaller dispersed grains, yet non-uniform grain sizes produce glass inhomogeneity and also impair optical transmittance. In contrast, the cross-sectional SEM micrograph of GCM940 prepared via two-step heat treatment (Fig. 2c) displays fine, homogeneously distributed grains embedded in the glass matrix. As illustrated in Fig. 2d, GCM940 exhibits an average grain size

of 1.69 μm, and this small grain size accounts for its enhanced optical transmittance. EDS elemental mapping (Fig. 2e) confirms good elemental uniformity, with Mg, Nb, O and Cr homogeneously distributed throughout the glass matrix. Fig. 2f presents the EDS elemental distribution maps of the scanned region, in which the molar fractions of Mg, Nb and O are 12.58%, 27.35% and 59.86%, respectively. The values are close to the atomic ratio of $MgNb_2O_6$, indicating the successful precipitation of $MgNb_2O_6$ crystals in the glass matrix.

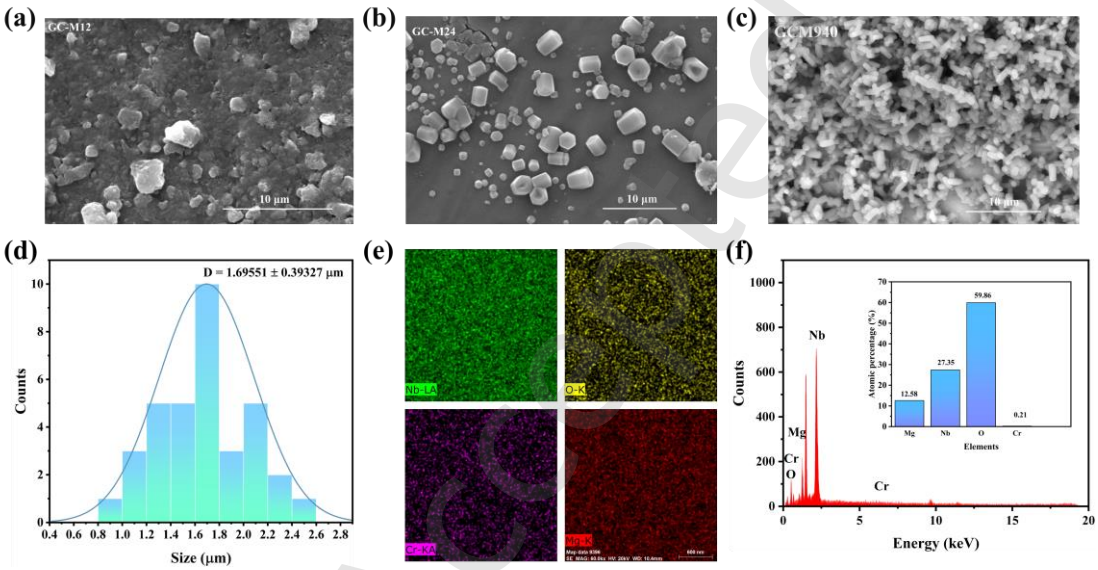


Fig. 2 SEM images of (a) GC-M12, (b) GC-M24. (c) The cross-sectional SEM image, (d) particle size distribution, (e) elemental mapping, and (f) EDS of GCM940.

### 3.3. $Cr^{3+}$ site occupancy in $MgNb_2O_6$

The PLE and PL spectra of GC-M24, as shown in Fig. 3a, were recorded using different excitation and emission wavelengths to investigate the fluorescence mechanism. Obviously, the PLE and PL spectra of GC-M24 exhibit different peak positions and both sharp and broadband features. Under excitation at 422 nm and 452 nm, emission peaks at 701 nm and 852 nm are observed, which are attributed to the spin-forbidden $^2E \rightarrow {}^4A_2$ transition and the spin-allowed $^4T_2 \rightarrow {}^4A_2$ transition of $Cr^{3+}$, respectively. Under excitation with these two different wavelengths, the emission spectra show different spectral shapes and variations in peak intensity, indicating the presence of two distinct $Cr^{3+}$ emission centers, similar results have been reported by Zhong et al. [23]. Since the $MgNb_2O_6$ crystal structure contains only one type of Mg site and one type of Nb site, it suggests that $Cr^{3+}$ may simultaneously occupy both lattice sites (denoted as Cr(1) and Cr(2)) and emit light at different

wavelengths. The aliovalent substitution of $Cr^{3+}$ for $Mg^{2+}$ ($Cr^{3+} \rightarrow Mg^{2+}$) and for $Nb^{5+}$ ($Cr^{3+} \rightarrow Nb^{5+}$) inherently requires charge compensation to maintain local electrical neutrality. Occupation of $Mg^{2+}$ sites by $Cr^{3+}$ generates excess positive charge, whereas occupation of $Nb^{5+}$ sites results in a deficit of negative charge. Therefore, $Cr^{3+}$ may simultaneously occupy both types of sites to achieve charge balance, as will be demonstrated later. The emission spectrum under 422 nm excitation was fitted with three Gaussian peaks, as shown in Fig. 3b. The peaks at 701 nm and 724 nm are attributed to Cr(1), probably corresponding to emission from Nb-site substitution, and the peak at 850 nm is attributed to Cr(2), probably corresponding to emission from Mg-site substitution. The crystal field strength is characterized by the crystal field splitting parameter $Dq = ze^2r^4/6R^5$, where $z$, $e$, $r$, and $R$ represent the anion charge, electron charge, d-wavefunction radius, and the distance between the central ion and ligands, respectively. Obviously, $Dq$ is inversely proportional to $R^5$. A weaker crystal field environment generally results in a broader emission spectrum and a longer emission wavelength. It is therefore speculated that the smaller Nb site corresponds to the Cr(1) center, while the larger Mg site corresponds to the Cr(2) center. The luminescence of $Cr^{3+}$ is significantly influenced by the crystal field strength, so it is necessary to determine the crystal field strength parameter ($Dq$) and the Racah parameter ($B$) of the host. The calculation formulas are as follows [24,25]:

$$10Dq = E(^4A_2 \rightarrow {}^4T_2) - \frac{\Delta S}{2} \tag{2}$$

$$\frac{Dq}{B} = \frac{15\,(x-8)}{x^2 - 10x} \tag{3}$$

$$x = \frac{E(^4A_2 \rightarrow {}^4T_1) - E(^4A_2 \rightarrow {}^4T_2)}{Dq} \tag{4}$$

$$\Delta S = E(^4A_2 \rightarrow {}^4T_2) - E(^4T_2 \rightarrow {}^4A_2) \tag{5}$$

Where $Dq$ represents the crystal field splitting strength, the Racah parameter $B$ reflects the strength of electron-electron repulsion within the 3d orbitals of $Cr^{3+}$. A higher $B$ value signifies stronger Coulombic repulsion, which favors a more ionic character in the $Cr^{3+}$-ligand bonds. The transition energies from the ground state $^4A_2$ to the excited states $^4T_2$ and $4T_1$ are denoted by $E(^4A_2 \rightarrow {}^4T_2)$ and $E(^4A_2 \rightarrow {}^4T_1)$, respectively, while $\Delta S$ corresponds to the Stokes shift, i.e., the energy separation between the excitation and emission peaks of the $^4A_2 \rightarrow {}^4T_2$ transition. The ratio $Dq/B$ quantitatively

describes the crystal-field strength; for a $d^3$ configuration ($Cr^{3+}$), the crossover point in the Tanabe-Sugano diagram occurs at $Dq/B$ = 2.3. Applying Eqs. (2)–(5) to the experimental data yields $Dq/B$ values of 2.41 for Cr(1) and 2.23 for Cr(2), confirming that $Cr^{3+}$ ions occupy both intermediate-field (Cr(1)) and weak-field (Cr(2)) sites simultaneously.

To further determine the lattice occupation sites of $Cr^{3+}$, Rietveld refinement was performed on the XRD data of the $Mg_2NbO_6$ GC and $Mg_2NbO_6$:$Cr^{3+}$ GC samples, as shown in Figs. 3d–e. The residual factors of the refinement results are within the acceptable error range, indicating that the refinement results are reliable. Fig. 3f shows a histogram of the changes in Mg-O and Nb-O bond lengths before and after $Cr^{3+}$ doping. Compared with the undoped sample, the Mg-O bond length decreases slightly after $Cr^{3+}$ doping, while the Nb-O bond length increases. The result may be attributed to the preferential substitution of $Cr^{3+}$ (with a smaller ionic radius) for $Mg^{2+}$ sites (with a larger ionic radius) in the lattice, leading to local lattice contraction. However, as the doping contents increase, the substitution of $Cr^{3+}$ for $Mg^{2+}$ sites causes a severe charge imbalance, thereby generating lattice defects. To maintain the electrical neutrality of the system, some $Cr^{3+}$ ions may instead occupy $Nb^{5+}$ sites. From the perspective of ionic radius, when $Cr^{3+}$ substitutes for $Nb^{5+}$, a shortening of the Nb-O bond length would be expected. Nevertheless, the refined Nb-O bond length shows an increasing trend, which may be attributed to the following mechanisms: on one hand, $Cr^{3+}$ ions occupying $Mg^{2+}$ sites exert a pulling effect on the surrounding [$NbO_6$] octahedra, causing lattice distortion; on the other hand, the ionic radius difference between $Cr^{3+}$ and $Nb^{5+}$ is relatively small, so the lattice contraction effect caused by $Cr^{3+}$ occupying $Nb^{5+}$ sites is not significant. Under the combined effect of the above multiple factors, the overall Nb-O bond length eventually increases. Due to the incorporation of $Cr^{3+}$ into the lattice, the unit cell volume of the $MgNb_2O_6$:$Cr^{3+}$ GC is smaller than that of the undoped $MgNb_2O_6$, which may be attributed to the substitution of $Cr^{3+}$ for $Mg^{2+}$ and $Nb^{5+}$, causing lattice contraction, further indicating that $Cr^{3+}$ enters the lattice. Detailed crystal structure parameters are listed in Table 2.

Table 2 Rietveld refinement results of XRD data for $MgNb_2O_6$ and $MgNb_2O_6$:0.1$Cr_2O_3$.

| | $MgNb_2O_6$ GC | $MgNb_2O_6$:$Cr^{3+}$ GC |
|---|---|---|
| *a*(Å) | 14.17631 | 14.17176 |
| *b*(Å) | 5.69472 | 5.69153 |
| *c*(Å) | 5.03159 | 5.03053 |

| | | |
|---|---|---|
| $V$(Å$^3$) | 406.201 | 405.757 |
| $R_{wp}$(%) | 5.69 | 5.8 |
| $\chi^2$ | 4.47 | 4.68 |

As shown in Figs. 3g–h, the fluorescence lifetime decay curves of GC-M24 indicate that under excitation at 422 nm and 452 nm and emission at 701 nm and 852 nm, the fluorescence decay time of Cr(1) is significantly longer than that of Cr(2), further confirming the presence of two emission centers for $Cr^{3+}$. Since the $MgNb_2O_6$:$Cr^{3+}$ GC does not show green coloration, XPS was further employed to determine the valence state of $Cr^{3+}$, as shown in Fig. 3i. The results obtained by fitting show that the binding energy of $Cr^{3+}$ is 576.37 eV, corresponding to the 2p orbital of $Cr^{3+}$, ruling out the possibility of valence variation of $Cr^{3+}$.

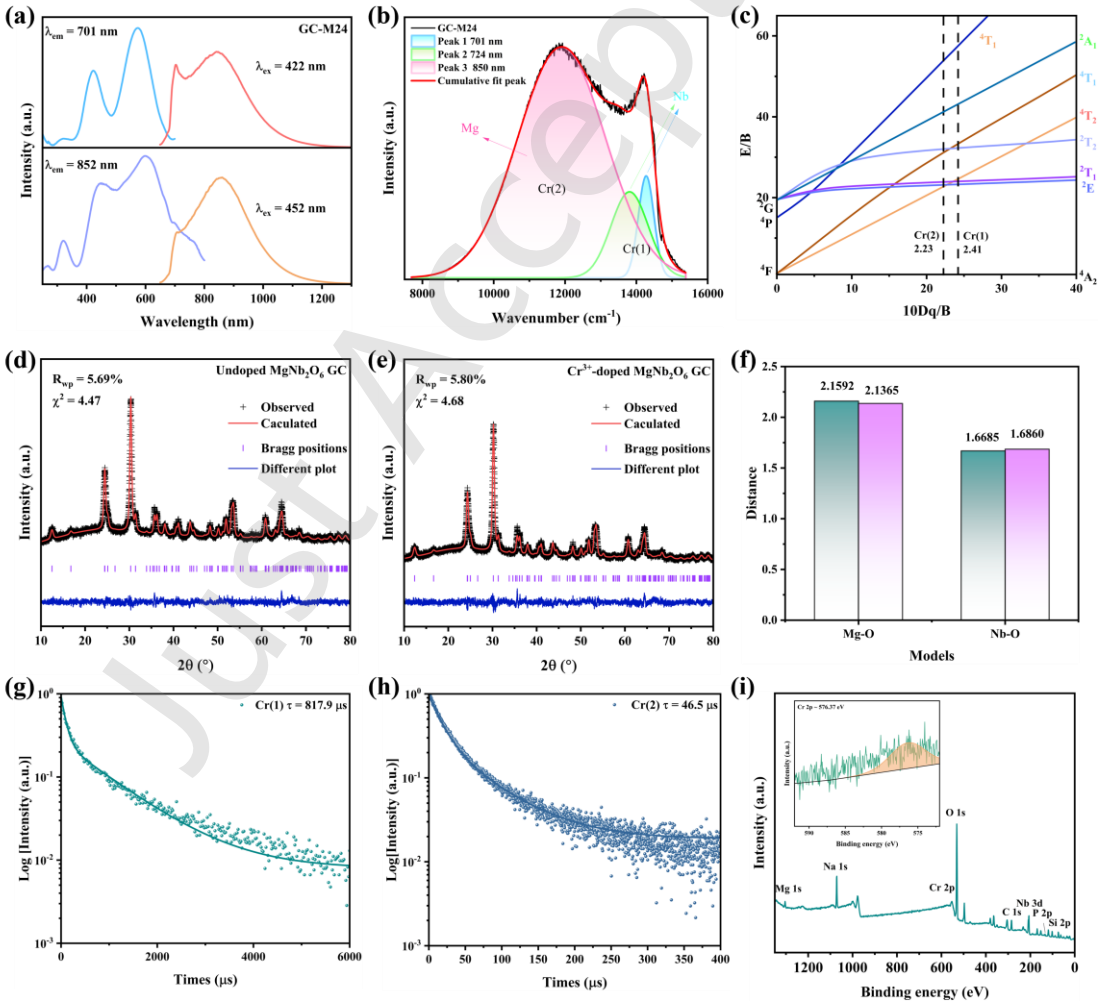


Fig. 3. (a) PLE and PL spectra of GC-M24. (b) Gaussian fitting of PL spectrum of GC-M24. (c) Tanabe-Sugano energy level diagram of Cr(1) and Cr(2). (d) Rietveld refinement plots of XRD data for $MgNb_2O_6$ GC and (e) $MgNb_2O_6$: $Cr^{3+}$ GC. (f) changes in Mg-O and Nb-O bond lengths. fluorescence lifetime decay curves of (g) Cr(1) and (h) Cr(2). (i) XPS of GC-M24.

**3.4. Luminescence properties**

The emission spectra of samples with different NT are shown in Fig. 4a. Under excitation at 452 nm, all samples exhibit broadband emission from 600 to 1300 nm with a full width at half maximum of 210 nm. The emission band is formed by the spectral superposition of two $Cr^{3+}$ emission centers. The narrowband emission at 701 nm corresponds to the spin-forbidden $^2E \rightarrow {}^4A_2$ transition of $Cr^{3+}$, while the broadband emission at 852 nm originates from the spin-allowed $^4T_2 \rightarrow {}^4A_2$ transition. Combined with the XRD results of Fig. 1f, as the NT increases from 670 ℃ to 750 ℃, the crystallinity of the samples gradually increases, and the emission intensity shows a slight enhancement, indicating that an appropriate increase in NT can improve the luminescence intensity of the GC samples. Fig. 4b shows the transmission spectra of MNO-670 to MNO-750, where the transmittance of the glass gradually decreases from approximately 70% to 50%, which will affect the transmittance in the subsequent crystallization stage. Compared with the excitation spectrum in Fig. 3a, the two excitation peaks are not obvious, as they are obscured by the absorption edge of the glass. In addition, with rising temperature, the baseline shifts to the right, which results from the formation of more $MgNb_2O_6$ crystals. This enhances the absorption of visible light, thereby promoting the redshift of the absorption edge. Considering both luminescence intensity and transmittance, 730 ℃ was selected as the optimal NT with a holding time of 12 h. Fig. 4c displays the PL spectra of the translucent GCs prepared at different crystallization temperatures. As the crystallization temperature increases from 820 ℃ to 960 ℃, the luminescence intensity increases almost linearly, reaching a maximum at 960 ℃. This result highlights the key role of crystallization temperature in regulating the crystallization degree of the GC and the local coordination environment of $Cr^{3+}$. Fig. 4d presents the PL spectra of GCs with $Cr^{3+}$ concentrations from 0.05 to 0.2 mol% under 452 nm excitation. As the $Cr^{3+}$ content increases, the emission peak shifts from approximately 850 nm to 874 nm, as shown in the inset. The redshift arises from the concentration-dependent site occupation of $Cr^{3+}$ ions in the $MgNb_2O_6$ lattice. As the concentration increases, the greater substitution of $Mg^{2+}$ by $Cr^{3+}$ results in a reduction of the crystal-field strength, shifting the emission to longer wavelengths. The emission intensity maximizes at 0.1 mol% and decreases beyond this concentration due to enhanced electric dipole-dipole interaction and increased non-radiative transition probability [26]. Fig. 4e shows the transmission spectra of the

samples from GCM820 to GCM960. As the crystallization temperature increases, the transmittance of the GC significantly decreases from 80% to 40%. In contrast to Fig. 4b, the spectra in Fig. 4e exhibit much stronger absorption in the 400–900 nm range, arising from enhanced precipitation and grain growth of $MgNb_2O_6$ microcrystals at elevated crystallization temperatures. However, the improved crystallinity and enlarged grain sizes further induce a redshift of the absorption edge. This edge overlaps with the absorption band of $Cr^{3+}$, resulting in a gradual reduction in the absorption intensity of the GCs [27]. To determine the optimum heat treatment temperature considering the trade-off between transmittance and luminescence intensity, the spectra of GCM920, GCM940, and GCM960 were tested after encapsulation with a 450 nm blue LED chip, and the results are shown in Fig. 4f. As the temperature increases, the spectra show a significant decrease in the blue light proportion, while the NIR light first increases and then decreases. GCM940 exhibits the maximum NIR light ratio. It is not difficult to understand that the decrease in GC transmittance improves the utilization efficiency of blue light, but also intensifies the scattering of NIR light. Therefore, GCM940 was selected as the optimal sample for subsequent testing and analysis.

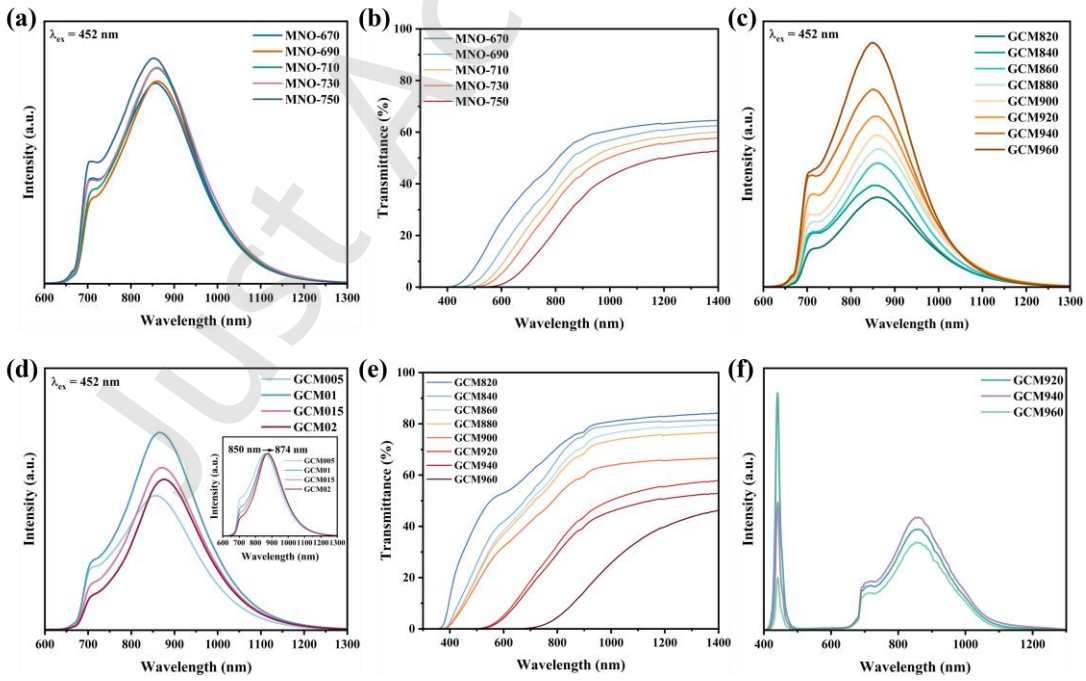


Fig. 4. (a) Emission spectra and (b) transmission spectra at different NT. Emission spectra (c) at different crystallization temperatures, (d) at different $Cr^{3+}$ doping concentrations (the inset is normalized spectra). (e) Transmission spectra at different crystallization temperatures. (f) Luminescence spectra of NIR LED devices from GCM920 to GCM960.

The temperature-dependent fluorescence spectra and integrated intensity of GCM940 are shown

in Figs. 5a–b. Obviously, the emission intensity decreases linearly with increasing temperature, retaining 67.5% and 51.9% of its initial intensity at 373 K and 423 K, respectively. Compared with previously reported NIR luminescent materials (as listed in Table 3), it exhibits a comparatively high resistance to thermal quenching. The thermal quenching activation energy ($\Delta E$) of the GC was calculated using the Arrhenius formula [28,29]:

$$I_T = \frac{I_0}{1 + cexp\left(-\frac{\Delta E}{kT}\right)} \tag{6}$$

where $I_T$ represents the luminescence intensity at temperature $T$, $I_0$ represents the luminescence intensity at the initial temperature, $k$ is the Boltzmann constant, and $c$ denotes a constant. Fig. 5c shows the plot of $\mathrm{Ln}(I_0/I_T - 1)$ versus $1/kT$, and the $\Delta E$ value is fitted to be 0.22 eV. In addition, the Huang-Rhys factor ($S$) related to the electron-phonon coupling (EPC) effect is fitted by Eqs. (7) [30]:

$$FWHM(T) = \sqrt{8\ln 2} \times \sqrt{S}\hbar\omega \sqrt{\coth\left(\frac{\hbar\omega}{2kT}\right)} \tag{7}$$

where $S$ represents the Huang-Rhys factor, $\hbar\omega$ denotes the average phonon energy, and $k$ is the Boltzmann constant. The fitted $\hbar\omega$ and $S$ values for GCM940 (Fig. 5d) are 62 meV and 5.43, respectively. Generally, $Cr^{3+}$ in the host material is considered to exhibit strong, intermediate, or weak EPC when $S > 10$, $1 < S < 10$, or $S < 1$, respectively [45]. Therefore, $Cr^{3+}$ in the GCM940 sample exhibits an intermediate EPC effect, indicating better thermal quenching resistance.

The Debye temperature and Vickers hardness are both important indicators for evaluating the structural rigidity of a material. The Debye temperature ($\Theta_D$) is calculated using the following equation [31]:

$$\Theta_D = \hbar v / k_B \tag{8}$$

where h is Planck's constant, $v$ is the maximum frequency of lattice vibrations in the solid, and $k_B$ is the Boltzmann constant. Moreover, since the Debye temperature is highly dependent on the molecular mass in the original formula (Eqs. (8)), its prediction of rigidity may be biased [31,32]:

$$\Theta_D = \frac{\hbar}{k_B}\left[6\pi^2 V^{\frac{1}{2}} N\right]^{\frac{1}{3}} \sqrt{\frac{B_H}{M}} f(v) \tag{9}$$

where $\hbar$ is the reduced Planck constant, $V$ is the unit cell volume, $N$ is the number of atoms in the unit

cell, $B_H$ is the bulk modulus of the crystal, $M$ is the molecular mass, and the expression for $f(v)$ is [33]:

$$f(v) = \left\{ 3 \left[ 2 \left( \frac{2}{3} \frac{1+v}{1-2v} \right)^{\frac{3}{2}} + \left( \frac{1}{3} \frac{1+v}{1-v} \right)^{\frac{3}{2}} \right]^{-1} \right\}^{\frac{1}{3}} \tag{10}$$

where $v$ is the Poisson's ratio [33].

$$\Theta_D = \frac{\hbar}{k_B} \left[ \frac{3n}{4\pi} \times \frac{N_A \rho}{M} \right]^{\frac{1}{3}} v_m \tag{11}$$

$$v_m = \left[ \frac{1}{3} \left( \frac{2}{v_s^3} + \frac{1}{v_1^3} \right) \right] \tag{12}$$

$$v_m = \left( \frac{G_H}{\rho} \right)^{\frac{1}{2}} \tag{13}$$

$$v_1 = \left( \frac{B_H + \frac{4}{3} G_H}{\rho} \right)^{\frac{1}{2}} \tag{14}$$

where $n$ is the number of atoms in the molecule ($n$ = 2 for NaCl), NA is Avogadro's number, $\rho$ is the density, and $G_H$ is the shear modulus. The Debye temperature and Vickers hardness of $MgNb_2O_6$ obtained by DFT calculation are 566.3 K and 7.78 GPa to 8.65 GPa, respectively.

Vickers hardness ($H_V$) is a widely adopted metric for evaluating the mechanical strength of superhard materials, as it reflects both the bond strength and bond density within a crystal lattice. Hence, $H_V$ can serve as an effective proxy for structural rigidity. Like the Debye temperature, $H_V$ can be estimated from elastic moduli obtained via first-principles calculations. However, unlike $\Theta D$, the empirical formula for $H_V$ has a much weaker dependence on atomic mass, thereby minimizing the weighting effect of constituent elements, whether light or heavy, on the estimated rigidity. Among the various semi-empirical models, Teter's formalism correlates $H_V$ with the shear modulus (G) and the ratio of G to the bulk modulus (B), as expressed below: [34]:

$$H_{V,Teter} = 0.92 \times k^{1.137} \times G^{0.708} \tag{15}$$

where $G$ is the shear modulus, $k = G/B$, and $B$ is the bulk modulus. In contrast, Vickers hardness has a very low dependence on atomic mass, thus it can better eliminate the interference of atomic mass and directly reflect the intrinsic rigidity of the material against thermal vibration. Therefore, $MgNb_2O_6$ possesses high Vickers hardness and Debye temperature, resulting in higher structural rigidity, and

consequently exhibits excellent thermal quenching resistance.

Quantum efficiency (QE) is a key parameter for evaluating luminescent materials. The internal quantum efficiency (IQE) of GCM940 was directly measured under 452 nm excitation using an integrating sphere (Fig. 5e). The internal quantum efficiency (IQE) can be calculated using the following equation [35]:

$$IQE = \frac{\int L_s}{\int E_r - \int E_s} \tag{16}$$

where $L_s$ is the emission intensity of the GC, and $E_r$ and $E_s$ represent the excitation spectra of the GC and the reference sample, respectively. According to Eqs. (16), the IQE of GCM940 is calculated to be 30.2%, and the value is a moderate level compared with other reports, as shown in Table 3. Fortunately, the external quantum efficiency (EQE) of 18.3% exhibits favorable characteristics. The result is attributed to the high absorptivity of up to 60.5%, attributed to the low light scattering caused by the microscale GC.

Table 3 Relevant properties of $Cr^{3+}$-doped NIR luminescent materials.

| Material | $\lambda_{ex}/\lambda_{em}$ (nm) | FWHM (nm) | IQE/EQE (%) | I@T (%) | Power (mW) | Ref. |
|---|---|---|---|---|---|---|
| $CaF_2:Cr^{3+}$ GC | 470/880 | 297 | 31.2/- | 40@100 | - | [36] |
| $Ba_2NaNb_5O_{15}:Cr^{3+}$ GC | 460/810 | 230 | 30.8/- | 30@100 | 131.7@230 mA | [14] |
| $(Al_{4-x}Ga_x)B_2O_9$ | 450/750 | 225 | 46/34 | 75@100 | 275@500 mA | [37] |
| $LiAl_5O_8$: $Cr^{3+}$ GC | 415/720 | - | 41.3/- | 67@100 | 137.1@300 mA | [38] |
| $Ca_2LaNbO_6:Cr^{3+}$GC | 434/735 | - | - | 85@150 | - | [15] |
| $AlNbO_4:Cr^{3+}$ phosphor | 450/880 | 242 | 37.4/21.8 | 40@100 | - | [39] |
| $Mg_4Nb_2O_9:Cr^{3+}$ phosphor | 468/920 | 164 | 67.1/26 | 10.5@150 | 62.4@320 mA | [40] |
| $Li_3Mg_2NbO_6:Cr^{3+}$ phosphor | 460/714 | 160 | - | 20@150 | 10@160 mA | [41] |
| $Ba_2LaNbO_6:Cr^{3+}$ phosphor | 324/681 | - | - | 10@150 | 2.3@300 mA | [42] |
| $CaMgSi_2O_6:Cr^{3+}$ phosphor | 450/785 | 138 | 25.1/- | 63@150 | 9@120 mA | [43] |
| $K_3AlF_6:Cr^{3+}$ phosphor | 450/770 | 220 | 25/- | - | 7@350 mA | [44] |
| $NaScP_2O_7:Cr^{3+}$ phosphor | 472/910 | 200 | 14.9/- | - | - | [45] |
| $NaScSi_2O_6:Cr^{3+}$ phosphor | 480/860 | 149 | 22.2/10.2 | 69@150 | 80@300 mA | [46] |
| $MgNb_2O_6:Cr^{3+}$ GC | 452/852 | 210 | 30.2/18.3 | 68@100 | 240.9@500 mA | This work |

Fig. 5f shows the decay curves of $Cr^{3+}$-doped GCs with different concentrations monitored at 852 nm under excitation at 452 nm. All decay curves are fitted with a bi-exponential mode, and the fluorescence lifetime ($\tau$) is calculated by the following formula [47,48]:

$$\tau = \frac{\int tI(t)dt}{\int I(t)dt} \quad (17)$$

where $I(t)$ signifies the emission intensity corresponding to the time $t$.

With increasing $Cr_2O_3$ content from 0.05 to 0.2 mol%, the fluorescence lifetime ($\tau$) gradually decreases from 47.2 to 44.1 μs. This concentration-dependent quenching behavior can be rationalized by the energy transfer mechanism among $Cr^{3+}$ ions. At low doping levels, the relatively large interionic separation suppresses non-radiative energy migration, allowing the excited electrons to relax predominantly via radiative recombination, which accounts for the longer observed lifetime. As the $Cr^{3+}$ concentration rises, the average distance between adjacent ions shrinks. Once this distance falls below a critical value, which corresponds to the optimal doping concentration for this host, the probability of resonant energy transfer increases markedly. Consequently, the excitation energy is channeled through non-radiative cross-relaxation pathways rather than being emitted as photons, leading to a progressive reduction in the measured lifetime. This trend is consistent with the concentration-induced emission peak redshift observed in Fig. 4d, further corroborating the enhanced interionic interaction at higher $Cr^{3+}$ loadings [27].

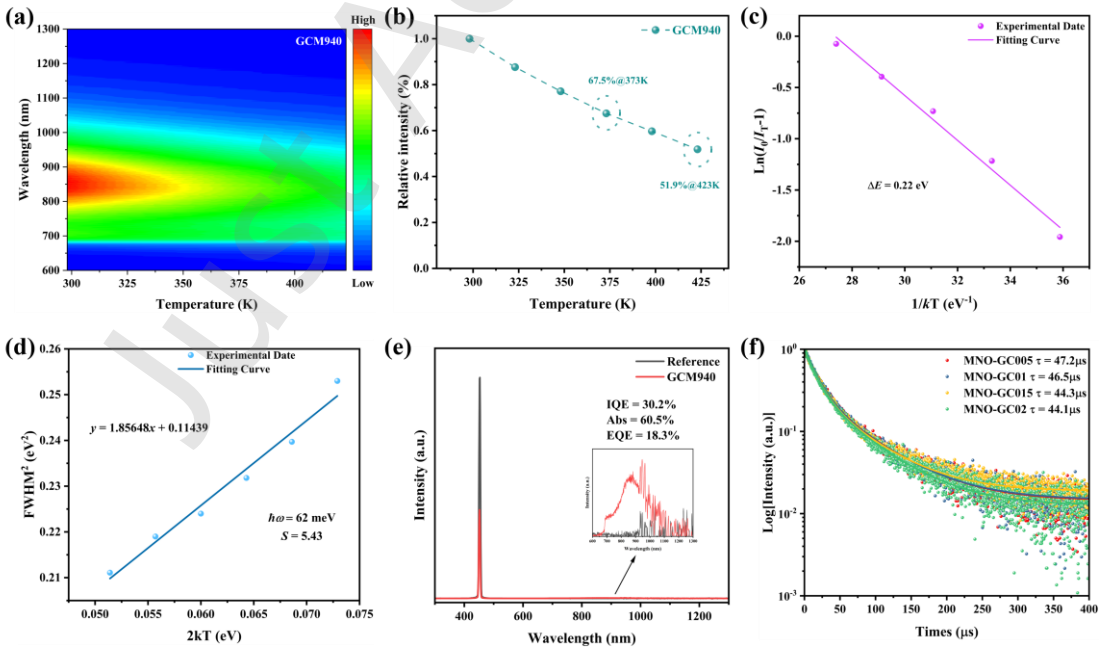


Fig. 5. (a) Thermal stability contour map and (b) relative integrated intensity variation curve of GCM940. (c) fitting result of $\mathrm{Ln}(I_0/I_T - 1)$ as a function of $1/kT$. (d) fitting result of $\mathrm{FWHM}^2$ as a function of $2kT$. (e) IQE of GCM940 sample. (f) decay curves of the GCs series.

### 3.5. NIR LED devices

To demonstrate the practical application value of the $MgNb_2O_6:Cr^{3+}$ GC, a NIR GC device was fabricated using a blue LED chip. Fig. 6a–b shows luminescence spectra of the NIR LED device composed of GCM940 and a 450 nm chip, and the output powers and conversion efficiencies under driving currents from 50 to 500 mA. The results demonstrate that an output power of 240.9 mW is achieved at a driving current of 500 mA, corresponding to competitive NIR output power compared with most reported values in other studies, as seen from Table 3 (the comparison is performed after eliminating the effects of sample thickness and human operational errors). The power conversion efficiency decreases from 8.1% to 6.3% as the increasing current from 50 at 500 mA, attributed to the efficiency drop of the LED chip. The emission peak at 440 nm originates from the blue LED chip, while the broadband emission covering 600–1300 nm is generated by the GC. The insets show photographs of the encapsulated device. Figs. 6c–e shows images of a medicine bottle, human fingers, the back of the hand, palm, blueberries, and a campus card under natural light and NIR light, respectively. Under NIR irradiation, the remaining content of the medicine bottle, the blood vessels at various positions of the human hand, the internal condition of good and bad blueberries, and the position of the chip inside the card can be clearly observed using a NIR camera. The results indicate that the device has application potential in night vision illumination, biomedicine, food testing, and anti-counterfeiting.

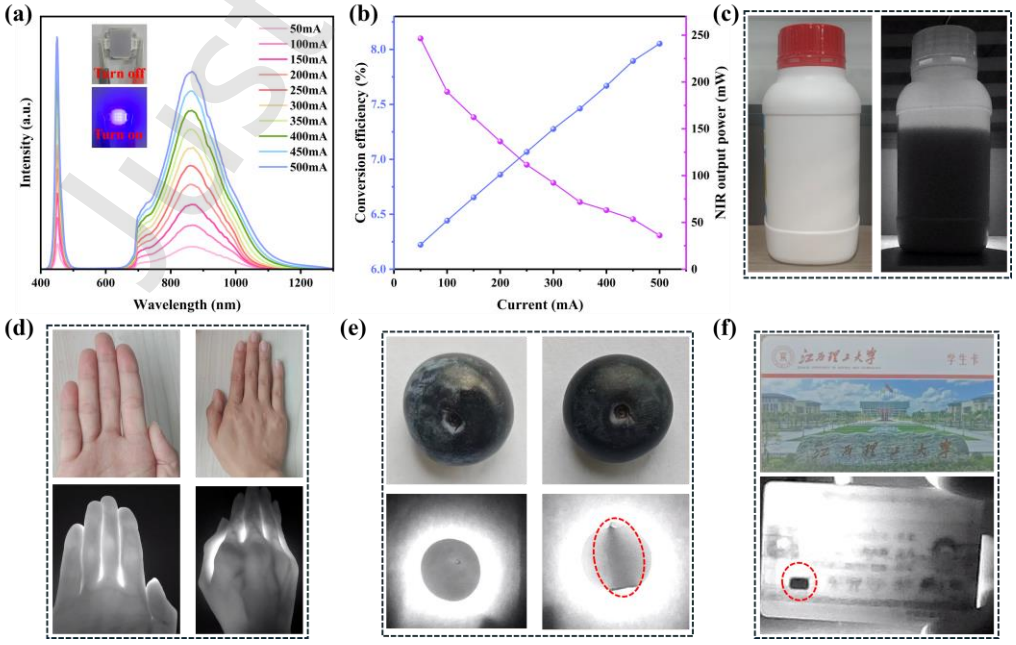


Fig. 6. (a) Luminescence spectra of the NIR LED device composed of GCM940 and a 450 nm chip

(inset shows a photograph of the device). (b) output powers and conversion efficiencies under driving currents from 50 to 500 mA. images of (c) a medicine bottle, (d) a human finger, backs of hands and palms, (e) a blueberry and (f) campus card under natural light and NIR light.

## 4. Conclusion

In summary, transparent $MgNb_2O_6:Cr^{3+}$ broadband NIR luminescent GCs were designed and prepared via a strategy of co-melting and controlled crystallization. At the optimal nucleation temperature of 730 ℃ and crystallization temperature of 940 ℃, the crystallinity, grain uniformity, and luminescence intensity of the material are significantly improved, while favorable optical transmittance is maintained. $Cr^{3+}$ simultaneously substitutes for $Mg^{2+}$ and $Nb^{5+}$, occupying the [$MgO_6$] and [$NbO_6$] octahedral sites, respectively, and resides in both intermediate and weak crystal field environments. The optimized GC yields broadband NIR emission covering 600–1300 nm with an FWHM of 210 nm. It achieves an external quantum efficiency (EQE) of 18.3% and retains 67.5% and 51.9% of its room-temperature luminescence intensity at 373 K and 423 K, respectively, revealing favorable resistance to thermal quenching. The NIR GC LED device fabricated by encapsulating the $MgNb_2O_6:Cr^{3+}$ GC with a blue LED chip shows significant application potential in biomedical diagnosis, night-vision illumination, food testing, and anti-counterfeiting.

**Author Information**

**Corresponding Author**

*E-mail: tea_xia@126.com, ye_xin_yu@126.com

Phone: +8613970736437.

**Present Address**

Jiangxi University of Science and Technology, Ganzhou 341000, China.

**Conflict of interest**

The authors declare no conflict of interest.

**Acknowledgments**

The work was supported by the National Natural Science Foundation of China (52062017) and Jiangxi Provincial Natural Science Foundation (20232BAB204013).

# References


[1] Yan WJ, Li T, Shi PH*, et al.* A NASICON-type structure $NaAlNb(PO_4)_3:Cr^{3+}$ phosphor with both high efficiency and thermal quenching resistance. *J Alloys Compd* 2026, **1067**: 188314.

[2] Zheng GJ, Xiao WG, Wu JH*, et al.* Glass-Crystallized Luminescence Translucent Ceramics toward High-Performance Broadband NIR LEDs. *Adv Sci* 2022, **9**: 2105713.

[3] Yang L, Zheng GJ, Liao C*, et al.* Glass-crystallized far-red-emitting ceramics for high-power, spectrally matched plant-growth light sources. *J Adv Ceram* 2025, **14**: 9221158.

[4] Qiao JW, Zhang S, Zhou XQ*, et al.* Near-Infrared Light-Emitting Diodes utilizing a Europium-Activated Calcium Oxide Phosphor with External Quantum Efficiency of up to 54.7%. *Adv Mater* 2022, **34**: 2201887.

[5] Huang JL, Fang WF, Xia LB. Ultra-broadband near-infrared emission of $AlNbO_4:Cr^{3+}$ transparent glass-ceramics. *J Non-Cryst Solids* 2025, **666**: 123720.

[6] Fu J, Zhang Y, Feng SW*, et al.* Biphasic $(Lu,Gd)_3Al_5O_{12}$ -based transparent nanoceramic color converters for high-power white LED/LD lighting. *J Adv Ceram* 2023, **12**: 2331-44.

[7] Rajendran V, Chang CY, Huang MH*, et al.* Chromium Cluster Luminescence: Advancing Near-Infrared Light-Emitting Diode Design for Next-Generation Broadband Compact Light Sources. *Adv Opt Mater* 2024, **12**: 2302645.

[8] Dang PP, Wei Y, Liu DJ*, et al.* Recent Advances in Chromium-Doped Near-Infrared Luminescent Materials: Fundamentals, Optimization Strategies, and Applications. *Adv Opt Mater* 2023, **11**: 2201739.

[9] Liu GC, Xia ZG. Modulation of Thermally Stable Photoluminescence in $Cr^{3+}$-Based Near-Infrared Phosphors. *J Phys Chem Lett* 2022, **13**: 5001-8.

[10] Lin H, Hu T, Cheng Y*, et al.* Glass Ceramic Phosphors: Towards Long-Lifetime High-Power White Light-Emitting-Diode Applications-A Review. *Laser Photonics Rev* 2018, **12**: 1700344.

[11] Gao Y, Murai S, Shinozaki K*, et al.* Phase-Selective Distribution of $Eu^{2+}$ and $Eu^{3+}$ in Oxide and Fluoride Crystals in Glass-Ceramics for Warm White-Light-Emitting Diodes. *ACS Appl Electron Mater* 2019, **1**: 961-71.

[12] Ji WB, Zhu FM, Gao Y*, et al.* Efficient $Ba_2NaNb_5O_{15}:Cr^{3+},Yb^{3+}$ nanocrystals embedded transparent glass-ceramics toward night-vision application. *Ceram Int* 2025, **51**: 32793-9.

[13] Ji WB, Zhu FM, Gao Y*, et al.* Near-Infrared Luminescent Transparent Glass-Ceramic Containing $Ba_{2-x}Sr_xNaNb_5O_{15}$ Solid-Solution Nanocrystals with Wavelength Tunability. *ACS Appl Mater Interfaces* 2025, **17**: 55026-33.

[14] Ji WB, Zhu FM, Gao Y*, et al.* Near-Infrared Luminescence of $Cr^{3+}$-Doped $Ba_2NaNb_5O_{15}$ Embedded in Transparent Glass-Ceramics as Solid-State Illumination for Night-Vision Imaging. *ACS Appl Mater Interfaces* 2025, **17**: 28366-73.

[15] Gao T, Chen QL, Wang N. Oxygen vacancy-engineered $Cr^{3+}:Ca_2LaNbO_6$ glass-ceramics via controlled crystallization: Dual enhancement of photoluminescence and magnetism. *J Alloys Compd* 2025, **1036**: 182189.

[16] Wang T, Zhang HB, Su CH*, et al.* Improving the luminescence, hardness and thermal stability of silicate glass for white LED by precipitation of $Ba_2YNbO_6$ crystals. *J Alloys Compd* 2022, **905**: 164221.

[17] Liang HZ, Luo ZW, Wu KP*, et al.* Structure and tunable broadband near-infrared luminescence of $Cr^{3+}$in borophosphate glass. *Ceram Int* 2022, **48**: 34617-26.

[18] Liu ZY, Wang B, Zhang K*, et al.* Near infrared persistent luminescence of transparent Zn-Ga-Ge-O:$Cr^{3+}$ glass ceramic for optical information storage. *Ceram Int* 2022, **48**: 3274-9.

[19] Pavlov RS, Marzá VB, Carda JB. Electronic absorption spectroscopy and colour of chromium-doped solids. *J Mater Chem* 2002, **12**: 2825-32.

[20] Yu DC, Ding QY, Shen TT*, et al.* Broadband short-wave near-infrared-emitting phosphor $MgNb_2O_6$:$Cr^{3+}$ for pc-LED applications. *Dalton Trans* 2024, **53**: 3702-12.

[21] Shi Y, Song XW, Han XX. Catalytic mechanism of iron oxide doping on the crystallization process of $Cr_2O_3$-containg glass ceramics. *J Non-Cryst Solids* 2021, **570**: 121002.

[22] Wang TZ, Wang YZ, Chen WB*, et al.* Crystallization of $Na_2SrGe_6O_{14}$:$Cr^{3+}$,$Yb^{3+}$ Glass Ceramics Enabling a Watt-Level Output Power NIR-I/NIR-II Lighting Source. *Laser Photonics Rev* 2024, **18**: 2300784.

[23] Zhong L, Xiang YF, Liu SW*, et al.* Valence and Site Engineering Enable Efficient Broadband Near-Infrared Emission at 960 nm in $Cr^{3+}$-Activated Forsterite. *Adv Mater* 2025, **37**: 2508768.

[24] Hayes W. Optical Spectroscopy of Inorganic Solids. *J Mod Opt* 1990, **37**: 1149-50.

[25] Zheng GJ, Lou CJ, Yuan ZY*, et al.* Rare-Metal-Free Ultrabroadband Near-Infrared Phosphors. *Adv Mater* 2025, **37**: 2415791.

[26] Wang BC, Yan C, Shen KW*, et al.* Luminescence enhancement of $Cr^{3+}$ doped garnet phosphor for high-performance LED towards smart NIR light source. *Ceram Int* 2023, **49**: 21864-71.

[27] Zhang SA, Long Y, Zhang PH*, et al.* Ultra-transparent β-$Ga_2O_3$:$Cr^{3+}$ glass-ceramics enabling high-efficiency true-transmission near-infrared light-emitting diodes. *J Adv Ceram* 2025, **14**: 9221075.

[28] Zhang LL, Wang DD, Liu F*, et al.* Minimizing Bond Angle Distortion to Improve Thermal Stability of $Cr^{3+}$ Doped Near-Infrared Phosphor. *Laser Photonics Rev* 2023, **17**: 2300092.

[29] Huang YP, Lv SC, Wang DZ*, et al.* Transparent Composite for Cooperative Near-infrared and X-ray Imaging. *Laser Photonics Rev* 2025, **19**: 2401593.

[30] Liu WY, Yuan LF, Wu HY*, et al.* Achieving broadband near-infrared emission with superior anti-thermal quenching by optimizing the excited-state population of $Cr^{3+}$ in $Gd_3ScGa_4O_{12}$ garnet phosphors. *Mater Horiz* 2024, **11**: 6399-407.

[31] Mahmood W, Sabieh Anwar M, Zia W. Experimental determination of heat capacities and their correlation with theoretical predictions. *Am J Phys* 2011, **79**: 1099-103.

[32] Anderson OL. A simplified method for calculating the debye temperature from elastic constants. *J Phys Chem Solids* 1963, **24**: 909-17.

[33] Xu SJ, Feng JH, Zhang DD*, et al.* Quantifying rigidity for thermally stable $Cr^{3+}$ phosphors. *Phys Chem Chem Phys* 2023, **25**: 29303-9.

[34] Tian YJ, Xu B, Zhao ZS. Microscopic theory of hardness and design of novel superhard crystals. *Int J Refract Met Hard Mater* 2012, **33**: 93-106.

[35] Xiao ZL, Qin SK, Guo X*, et al.* Efficient and broadband near-infrared emission of $Cr^{3+}$-doped glass-ceramics for near-infrared light sources applications. *J Lumin* 2022, **247**: 118907.

[36] Ren J, Zhu FM, Gao Y*, et al.* Ultra-broadband near-infrared emission of $Cr^{3+}$-containing oxy-fluoride glass-ceramics. *Ceram Int* 2024, **50**: 31474-81.

[37] Zhang YM, Chen Z, Li RZ*, et al.* $Ga^{3+}$ Cation-Directed Microstructural Engineering of Glass-Ceramics Unlocks High-Power NIR LEDs. *Laser Photonics Rev* 2026, **20**: e03261.

[38] Ji WB, Zhu FM, Gao Y*, et al.* $Cr^{3+}$-doped $LiAl_5O_8$ nanocrystals embedded in transparent glass-ceramic with high NIR PLQY and excellent thermal stability. *Ceram Int* 2025, **51**: 41716-22.

[39] Lyu KN, Liu GC, Molokeev MS*, et al.* Double-Site Occupation Triggered Broadband and Tunable NIR-I and NIR-II Luminescence in $AlNbO_4:Cr^{3+}$ Phosphors. *Adv Phys Res* 2023, **2**: 2200056.

[40] Ding QY, Wu JC, Yu DC*, et al.* Broadband short-wave infrared $Mg_4Nb_2O_9:Cr^{3+},Li^+$ phosphor for nondestructive safety detection and biomedical imaging. *J Mater Chem C* 2024, **12**: 2184-93.

[41] Xiao F, Xie CN, Xie SK*, et al.* Multi-site $Cr^{3+}$ occupation-related broadband NIR luminescence in $Cr^{3+}$-doped $Li_3Mg_2NbO_6$. *CrystEngComm* 2021, **23**: 5585-94.

[42] Wang YN, Sun YX, Xu Z*, et al.* Two-Site Occupation for Constructing Double Perovskite $BaLaMgNbO_6:Cr^{3+}$ Ultrabroadband NIR Phosphors. *Inorg Chem* 2024, **63**: 8899-907.

[43] Dong XQ, Chen ZB, Liu LH*, et al.* Tuning the emission half-peak width of $CaMgSi_2O_6:Cr^{3+}$from 138 nm to 393 nm by controlling the $Cr^{3+}$concentration. *J Alloys Compd* 2024, **981**: 173746.

[44] Lee C, Bao Z, Fang MH*, et al.* Chromium(III)-Doped Fluoride Phosphors with Broadband Infrared Emission for Light-Emitting Diodes. *Inorg Chem* 2020, **59**: 376-85.

[45] Zhang XZ, Dai PP, Wen DW. Ultra-broadband of up to 200 nm near-infrared phosphors based on one-site occupation strategy for multipurpose applications in light-emitting diodes. *Ceram Int* 2023, **49**: 4881-8.

[46] Yan Y, Shang MM, Huang S*, et al.* Photoluminescence Properties of $AScSi_2O_6:Cr^{3+}$ (A = Na and Li) Phosphors with High Efficiency and Thermal Stability for Near-Infrared Phosphor-Converted Light-Emitting Diode Light Sources. *ACS Appl Mater Interfaces* 2022, **14**: 8179-90.

[47] He GL, Chen JY, Li LJ*, et al.* $Cu^+$-doped oxyfluoride glass with anti-thermal-quenching luminescence for X-ray imaging and WLED. *J Adv Ceram* 2025, **14**: 9221116.

[48] He GL, Li LJ, Chen JY*, et al.* A Thermal Stable Multi-Functional $Cu^+$-doped Glass for High-Resolution X-Ray Imaging and Full-Spectra Lighting. *Laser Photonics Rev* 2025, **19**: e00396.